THE JOURNAL OF
PHYSICAL CHEMISTRY A

Article

pubs.acs.org/JPCA

Interaction of Helium Rydberg State Molecules with Dense Helium

Nelly Bonifaci,[†] Zhiling Li,[‡] Jussi Eloranta,[¶] and Steven L. Fiedler*[,§]

[†]G2ELab-GreEn-ER, Equipe MDE, 21 avenue des Martyrs, CS 90624, 38031 Grenoble Cedex 1, France
[‡]Guizhou Institute of Technology 1 Caiguan Road, 550003 Guiyang, China
[¶]Department of Chemistry and Biochemistry, California State University at Northridge, 18111 Nordhoff St., Northridge, California 91330, United States
[§]Department of Biology and Chemistry, Fitchburg State University, 160 Pearl St., Fitchburg, Massachusetts 01420, United States

Supporting Information

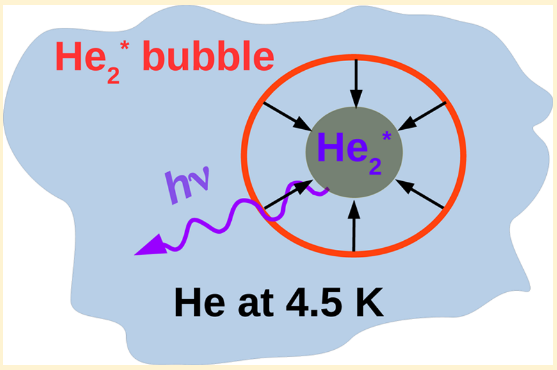

ABSTRACT: The interaction potentials of the He_2^* excimer, in the $a^3\Sigma_u$, $b^3\Pi_g$, $c^3\Sigma_g$, and $d^3\Sigma_u$ electronic states with a ground state helium atom are presented. The symmetry of the interaction potentials closely follows the excimer Rydberg electron density with pronounced short-range minima appearing along the nodal planes of the Rydberg orbital. In such cases, a combination of the electrostatic short-range attraction combined with Pauli repulsion leads to the appearance of unusual long-range maxima in the potentials. Bosonic density functional calculations show that the ^3d state excimer resides in a localized solvation bubble in dense helium at 4.5 K, with radii varying from 12.7 Å at 0.1 MPa to 10.8 Å at 2.4 MPa. The calculated $^3d \rightarrow {}^3b$ pressure-induced fluorescence band shifts are in good agreement with experimental results determined by application of corona discharge. The magnitude of the spectral shifts indicate that the observed He_2^* molecules emit from dense helium whereas the corresponding fluorescence signal from the discharge zone appears quenched. This implies that fluorescence spectroscopy involving this electronic transition can only be used to probe the state of the surrounding medium rather than the discharge zone itself.

INTRODUCTION

Many studies have been published on the conduction of dielectric liquids, e.g., refs 1−5. and references therein. It is, however, still difficult to predict the behavior of these liquids in high electric fields, in particular, breakdown characteristics, without having to recourse to numerous and expensive experimental investigations.[6] The electric breakdown of liquids consists of a complex sequence of correlated events[7−10] and the investigation of such processes requires the application of high electric fields, which can be achieved, for example, by corona discharge in the liquid. The corona discharge method is technically simple and can be used to interrogate mechanistic aspects of liquid breakdown. It has been determined that the initial localized discharge in the liquid phase is linked to ionization and excitation processes of the medium, which is subsequently followed by liquid heating and cavity formation.[11] However, salient physical parameters of the discharge zone, such as the density and temperature as well as the ionization coefficient of the liquid, are still largely unknown. The lack of this information is an obstacle for realistically modeling the discharge event. In gases, a good understanding of the discharge phenomena was obtained by using spectroscopic diagnostic techniques to measure the relevant discharge parameters.[12−14] These parameters were deduced from a detailed spectral analysis of the light emitted by the discharge. However, the application of the same technique in dielectric liquids is facing difficulties due to the high density present inside the discharge cavity.

In addition to possible fluorescence quenching, the influence of impurities, such as water and other polar molecules, become increasingly pronounced at higher densities. Moreover, the organic dielectric liquids that are currently employed to study the electric breakdown process undergo fragmentation due to the discharge, which further complicates the data analysis.[15−17] An effective way to study electric discharge events and extract relevant parameters in the liquid phase is to characterize such phenomena in a chemically inert monatomic fluid. To this end, liquid helium is an attractive candidate as it possesses rich fluorescence spectroscopy and contains practically no contaminants. The present work assesses the suitability of fluorescence spectroscopy to determine the physical parameters associated with corona discharge in dense helium, as a function of pressure and temperature.

Received: August 19, 2016
Revised: October 3, 2016
Published: October 26, 2016

Downloaded via FITCHBURG STATE UNIV on January 11, 2019 at 17:35:44 (UTC).
See https://pubs.acs.org/sharingguidelines for options on how to legitimately share published articles.

ACS Publications © 2016 American Chemical Society

DOI: 10.1021/acs.jpca.6b08412
J. Phys. Chem. A 2016, 120, 9019−9027

■ EXPERIMENT

The experimental setup, as described in greater detail in ref 18, consists of a helium cryostat that allows measurements to be taken from ambient temperatures down to 4.2 K. Briefly, a beryllium copper cell equipped with sapphire windows was attached to the cryostat cold head, which allowed optical measurements up to 10 MPa pressure. The temperature inside the cell was measured with a germanium sensor (LakeShore GR-200A-2500) with an accuracy of ±0.5 mK and pressure by a capacitance manometer (MKS Instruments Micro Baratron model 890B-33PCB2GK).

The cell was first evacuated using a turbo molecular pump down to 10^{-4} Pa and then filled with ultra pure helium (N60 l'Air Liquide; impurity concentration of less than 0.1 ppm of O_2). Prior to entering the cell, helium gas was passed through a series of liquid nitrogen immersed traps, which were filled with a mixture of molecular sieves (3−10 Å) and activated charcoal, with the latter prepared under vacuum for 3 days at 350 °C.

The point electrode placed inside the cell was made of electrolytically etched 1 mm diameter tungsten wire. Etching reduced the tip diameter to 0.45−2.5 μm, which was determined by an electron microscope (Jeol JSM 5600LV). The plane electrode was made of copper and located 8 mm away from the point electrode. All electrodes were insulated with Macor ceramic. The point electrode was either negatively or positively polarized by a stabilized high voltage dc power supply (Spellman RHSR/20PN60). The positive and negative corona discharges were driven by positive or negative point electrode polarity, respectively. The current (0.1−1 μA in the liquid phase) and voltage characteristics were measured by using a Tektronix TDS540 oscilloscope and a Keithley 610C ammeter. The corona discharge in this geometry is axially symmetric and appears as a luminous spherical discharge zone (ionization region) localized near the point electrode. The light originating from this zone was collected by two quartz lenses with focal lengths of 100 mm and 200 mm onto the entrance slit of a spectrograph (Acton Research Corporation 300i equipped with gratings 150 g/mm, 1200 g/mm blazed at 750 nm, and 1200 g/mm blazed at 300 nm). A liquid nitrogen cooled charge coupled device (CCD; Princeton Instruments model 2D-CCDTKB-UV/AR) was placed at the exit plane of the spectrograph. The noise level of this CCD detector was determined by the read-out noise as the dark current was less than 1 e/pixel/h at 153 K.

The wavelength and the intensity response of the detection system was calibrated by using low pressure helium (Lot Oriel SS.SPEC.He.10.0) and tungsten ribbon lamps. Line broadening due to the instrument response (1200 g/mm grating) was estimated from the 706 nm helium line as 0.12 nm.

■ THEORY

Excimer-Atom Pair Potentials. Triplet state potential energy curves were calculated to assess the interaction of the He_2^* excimer in the presence of a third, impinging, helium atom in the ground, ^1S, electronic state. Henceforth, the triatomic potentials will be denoted by the diatomic excimer state at the asymptotic separation limit with respect to the third atom. The ground state potential, a($^3\Sigma_u$), was calculated by the coupled-cluster based, CC3 approach, which employed iterative, partial triple excitations.[19,20] A restricted open shell Hartree−Fock calculation served as the reference for the CC3 wave function. Excited state energies for the b($^3\Pi_g$), c($^3\Sigma_g$), and d($^3\Sigma_u$) excimer states were determined using the equation-of-motion CC3 approach (EOM-CC3). Basis set superposition error (BSSE) was addressed by counterpoise correction,[21] which was allowable as the EOM-CC3 approach is size consistent. All pair potential calculations were performed using the Psi4 software package, version 0.3.[22]

The two basis sets employed to calculate the He_2^*−He triplet potentials have previously shown to be capable of providing sufficient accuracy to match absorption and emission spectra from atomic[18,23] and diatomic[24] helium Rydberg states. The smaller basis set, denoted in ref 24 and this study as "*", was originally developed by Sunil et al.[25] and was subsequently modified to increase accuracy.[24] The larger basis, denoted in ref 23. and in this study as "**", was originally developed by Deguilhem and Gadea,[26] and was subsequently parsed to increase functionality.[23] To avoid a linear dependency in the fully uncontracted basis set ** from ref 23, a diffuse *p*-Gaussian with exponent 0.006 was eliminated and the two *f* basis functions were dropped to reduce the computational time. The parameters for basis set **, as used in this study, are specified in Table 1.

Table 1. Uncontracted Gaussian Basis Set Exponents for Basis Set **

s	p	d
50000, 10000, 2000, 1000, 500, 200, 100, 50, 20, 10, 5, 2, 1, 0.5, 0.2, 0.1, 0.055, 0.02, 0.011, 0.006	50, 10, 5, 2, 1, 0.5, 0.2, 0.1, 0.05, 0.025, 0.012	5, 0.27, 0.11, 0.05

For closure, the excimer−helium pair potentials were calculated for both linear and perpendicular (*T*) orientations of the He_2^* quantization axis with respect to position of the third, ^1S, He atom. Calculations for both orientations employed the C_{2v} point group. The *T*-orientation calculation included consideration of both, nondegenerate, ^{3}b-states with π_u highest occupied molecular orbital (HOMO) of the excimer aligned (B_1) and oriented perpendicular (A_2) to the impinging ground state He atom. The helium atoms in the excimer were centered about the origin and separated from each other by the equilibrium bond distance of 1.05 Å.[23]

Bosonic Density Functional Theory Calculations. To model the distribution of liquid helium around He_2^* molecular excimers, the Orsay−Trento (OT) density functional theory (DFT) method was employed, which includes static thermal corrections up to 3.0 K.[27,28] Since the calculations were carried out in imaginary time, the backflow functional of OT was not included. Furthermore, the effect of the kinetic energy correlation term in OT appeared negligible and was therefore not considered. This basic form of OT functional has been shown to be able to model solvation of several types of impurities, e.g., electron,[29−32] He*,[18] halogen anions,[33] and Ba^+ cations.[34] Impurities that exhibit strong binding with helium typically require inclusion of the density cutoff functional,[30,34] but the He_2^*−He potentials employed do not possess such binding, with the exception of short-range pocket present for some excimer states. This excimer−liquid interaction is incorporated in the calculations as an external potential, which involves integration over the zero-point density of the excimer.[18]

The OT-DFT calculation numerically solves the coupled nonlinear Schrödinger equations for the excimer and superfluid helium[29−32] in three-dimensional space by employing the Crank−Nicolson method combined with the operator splitting technique.[35−38] In this work, a 256 × 256 × 256 Cartesian grid with a 1.0 bohr spatial step length was employed for both grids representing the liquid order parameter and the He_2^* zero-point wave function. The ground state solution for the system was obtained by propagating the equations in imaginary time.[35,36] A time step of 20 fs (5 fs for real time dynamics calculations) and 200 iterations were sufficient to reach convergence. This criterion was selected by observing the changes in both the liquid density around the excimer as well as the evolution of the OT energy density.

The linear dipolar fluorescence spectrum between two states, e.g., He_2^* ^{3}d → ^{3}b, can be obtained from the time-dependent response of first order polarization, $P^{(1)}(t)$, through Fourier transformation.[39] Unfortunately, this function depends on the true many-body wave function of the helium bath and therefore it cannot be directly obtained from OT-DFT. In this work, we have employed the approach developed in our earlier work,[18,40,41] which allows approximate evaluation of first order polarization at excitation angular frequency ω:

$$P^{(1)}(t) \propto i \int_0^t \exp\left(-\frac{i}{\hbar}\int_{t'}^{t} E_{\text{ext}}(t'')\, \mathrm{d}t'' - i\omega t'\right) \mathrm{d}t' + \text{CC} \tag{1}$$

where CC stands for the complex conjugate of the preceding term and $E_{ext}(t)$ is the energy gap determined by the excimer−bath interaction energies for the ground (g) and excited (e) electronic states:

$$\begin{aligned} E_{\text{ext}}(t) = {}& \iint \rho_{\text{e}}'(R, 0) V_{\text{e}}(|R - r|) \rho_{\text{e}}(r, 0)\, \mathrm{d}^3r\, \mathrm{d}^3R \\ & - \iint \rho_g'(R, t) V_g(|R - r|) \rho_g(r, t)\, \mathrm{d}^3r\, \mathrm{d}^3R \end{aligned} \tag{2}$$

where V_e is the excited state pair potential (e.g., $He_2^*(^3d)-He$), V_g is the ground state pair potential (e.g., $He_2^*(^3b)-He$), and $\rho'_{e/g}$ and $\rho_{e/g}$ correspond to He_2^* and liquid helium densities around the excited and ground state excimer, respectively. Note that only the second term in eq 2, which requires real time propagation of the system, is responsible for dynamic line broadening.

For He_2^* ^{3}d → ^{3}b fluorescence, the experimental linewidths are only available at low pressures and hence the calculated lineshift is the most important quantity that can be compared directly with experiments. Eq 1 does not include electronic dephasing, which can be included phenomenologically by a decaying exponential function:[41]

$$\bar{P}^{(1)}(t) = \mathrm{e}^{-t/\tau} P^{(1)}(t) \tag{3}$$

Here τ represents the dephasing time constant. In practice, the value of τ controls the time that the final state dynamics contributes to the line shape. For small values of τ, a structureless broad line is obtained whereas discrete lines may appear with larger τ values.[40,41] The fluorescence spectrum is finally obtained by Fourier transforming eq 3. To simplify eq 1, we have approximated the fluorescence spectrum by calculation of the power spectrum of eq 2. Finally, we note that all the triatomic state potentials correlated with the ^{3}b state appear essentially flat at distances relevant to ^{3}d state excimer solvation. According to eq 2, only the upper state potential (i.e., $He_2^*(^3d)-He$) contributes to the fluorescence band shift provided that τ remains sufficiently small. For long τ, the bound regions of $He_2^*(^3b)-He$ potentials could provide additional line broadening and shift.

RESULTS AND DISCUSSION

He_2^*−He Pair Potentials. The triplet state eigenenergies of an isolated He_2^* excimer are perturbed by the presence of an additional helium atom, as demonstrated in Figures 1 and 2.

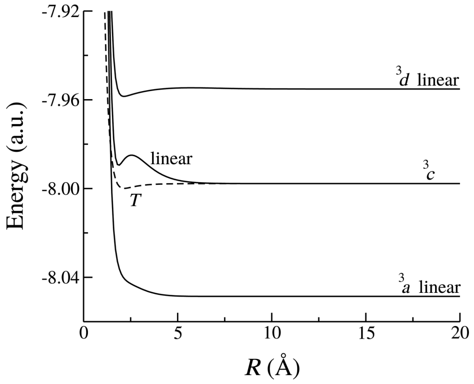

Figure 1. Overview of low-lying $^3A_1$ states of He_2^*−He in the C_{2v} point group. The He_2^* excimer (bond length fixed at 1.05 Å) was oriented as indicated: aligned (linear) or perpendicular (T) with respect to the asymptotically impinging He(^1S) atom. The data were obtained from EOM-CC3 calculation employing basis set *.

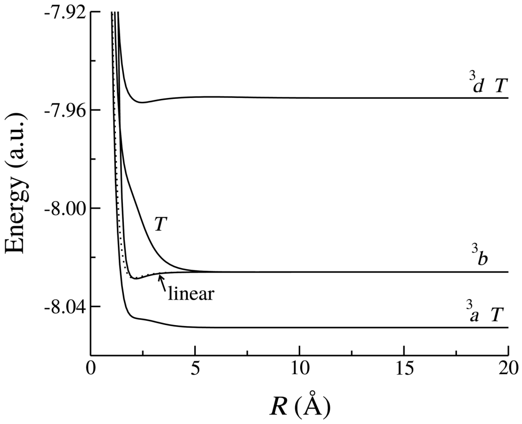

Figure 2. Overview of low-lying $^3B_1$ states of He_2^*−He in the C_{2v} point group. The He_2^* excimer (bond length fixed at 1.05 Å) was oriented as indicated: aligned (linear) or perpendicular (T) with respect to the asymptotically impinging He(^{1}S) atom. For completeness, a second ^{3}b state in the T-orientation is shown, which possesses an A_2 symmetry (dotted line). The data were calculated using EOM-CC3 and basis set *.

The excimer−atom potential profiles can be qualitatively rationalized by the electron density of the Rydberg orbital.[42] The symmetry of the valence states of He_2^*−He in the C_{2v} point group are determined by the symmetry of the Rydberg orbital on the excimer. This holds, since the unpaired valence electron in He_2^+ exists on the $1\sigma_u$ orbital, which belongs to the A_1 irreducible representation in C_{2v}. As such, the symmetry of the Rydberg electron in He_2^* denotes the symmetry of the molecule due to direct product rules and the fact that the third, impinging, He atom is a complete shell, i.e., the impinging atom itself has an A_1 symmetry.

The following discussion delineates the triatomic, He_2^*−He potentials, shown in Figures 1 and 2, with respect to the corresponding excimer states. As the ^{3}a Rydberg orbital is nearly isotropic, only minor differences are present in the respective pair potentials between the linear and *T*-orientations (*cf.* Figure 3). As previously determined,[42] the linear potential is slightly more repulsive than the *T*-potential. Although the ^{3}a state potentials are largely repulsive, they exhibit a small long-range minimum, *ca.* 1 cm^{-1}, situated around 7.3 Å (see Table 2). The calculated minimum distances of the ^{3}a-state are shorter by more than 0.5 Å and have deeper binding of up to a factor three to that calculated previously by CCSD(T) with an aug-cc-pV6Z basis.[42] Note that such a small binding energy has negligible contribution to the overall excimer solvation energy in liquid helium; i.e., $He_2^*(^3a)$ is a heliophobic species.

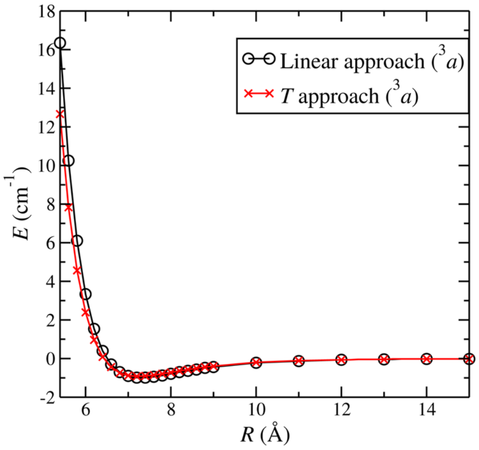

Figure 3. $He_2^*(^3a)$−He potentials from EOM-CC3/basis ** calculation. Linear and *T*-orientations are represented by (°) and (*), respectively.

The excimer−atom potentials associated with the ^{3}b state are more nuanced than that of the ^3a state due to the inherent anisotropy in the morphology of the π_u Rydberg orbital (see Figure 4). This yields three distinct molecular coordinates: (i) a linear He_2^* excimer orientation with the impinging helium atom approaching along the excimer quantization axis (z), (ii) a *T*-orientation of the excimer with the impinging atom approaching along the x coordinate, which corresponds to an A_2 representation in the C_{2v} group, and (iii) a *T*-orientation of the excimer with the impinging atom approaching along the y-coordinate, which has a B_1 molecular symmetry in C_{2v}. The decreased electron density along the nodal plane of the Rydberg molecular orbital "belt", i.e., the xz-plane in Figure 4a, results in decreased short-range repulsion between the excimer and the atom. Thus, the belt approaches encounter reduced repulsion with respect to the "head-on", *T*-orientation, approach along the y-axis. These belt state potentials also contain deep, short-range binding, due to deshielding of the He_2^+ excimer core, at 2.1 and 2.2 Å with binding energies of 535 and 594 cm^{-1}, respectively. The "head-on" *T*-orientation with B_1 symmetry is largely repulsive, with a shallow binding of less than 1 cm^{-1} at 8.2 Å. The ^{3}b belt states did not possess any equivalent long-range minima.

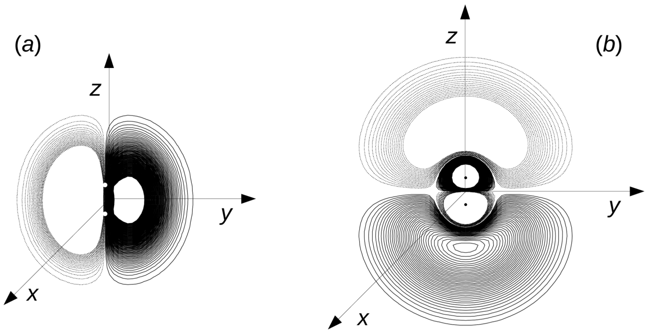

Figure 4. HOMO canonical molecular Rydberg orbitals of He_2^* in the ^{3}b- and ^{3}c-states, placed (a) left and (b) right, respectively. The position of the nuclei, represented as filled circles vertically centered about the origin (along z-axis), are colored white for the b-state and black for the c-state. See also refs 24 and 42 for natural Rydberg orbital and electron density contour plots of additional states.

As with the case of the ^{3}b state, the ^{3}c ($^3\Sigma_g$) state is also defined by a Rydberg HOMO that resembles an atomic p-orbital, Figure 4b. The potential defined by the linear excimer orientation (see Figure 1), contains a very shallow minimum of 0.4 cm^{-1} at 10 Å and a gradual repulsive wall starting at *ca.* 5 Å, which is similar in appearance to the "head-on", *T*-orientation of the B_1, ^{3}b state potential. Proceeding inward on the linear ^{3}c potential, a deep short-range pocket exists at 1.9 Å due to the presence of a radial node, which is visible in Figure 4b. The outer and inner minima are separated by a 2805 cm^{-1} energy barrier centered at 2.5 Å. As shown in Figure 1, the *T*-orientation of the ^{3}c state possesses the general form of the "belt" potentials of the ^{3}b state and has a minimum of 395 cm^{-1}

Table 2. Survey of He_2^*−He Triplet State Potentials in C_{2v} for the Linear (L) and T-Orientations (T)[a]

state	sym	r_e (Å)	D_e (cm^{-1})	r_b (Å)	E_b (cm^{-1})	r'_e (Å)	D'_e (cm^{-1})	E (10^3 cm^{-1})
^{3}d L	A_1	2.1	725	5.8	94.9	15.0	0.07	20.37
^{3}d T	B_1	2.4	394	5.8	79.4	15.0	0.05	20.37
^{3}c L	A_1	1.9	980	2.5	2805	10.0	0.43	11.15
^{3}c T	A_1	2.4	395					11.15
^{3}b L	B_1	2.2	594					4.87
^{3}b T	A_2	2.1	535					4.87
^{3}b T	B_1	8.2	0.64					4.87
^{3}a L	A_1	7.4	0.98					0
^{3}a T	B_1	7.2	0.93					0

[a] Potentials calculated by EOM-CC3 with basis ** except for italicized values indicating potentials calculated with basis *. Terms r_e and D_e denote equilibrium separation and binding energy respectively, and r_b and E_b indicate the barrier position and height with respect to the asymptote. The prime values: r'_e and D'_e pertain to a second minima, and the excitation energy, E, is the excimer excitation energy calculated with respect to the asymptotic limit of the ^{3}a state.

DOI: 10.1021/acs.jpca.6b08412
J. Phys. Chem. A 2016, 120, 9019−9027

at 2.4 Å, which is bound by a hard repulsive wall at short distances.

The ^{3}d state possesses a nearly isotropic s-type Rydberg orbital. An extremely small long-range binding was calculated at 15 Å of 0.07 and 0.05 cm^{-1} for the *T*- and linear orientations, respectively. More prominently, a radial node in the HOMO results in an energy barrier at 5.8 Å of 79 and 95 cm^{-1} for the linear and *T*-orientations, respectively. A deep pocket exists for both orientations between the barrier and the hard inner repulsive wall. The inner minimum of the linear geometry is located at 2.1 Å with a depth of 725 cm^{-1} and for the *T* geometry at 2.4 Å and 394 cm^{-1}. The $\mathrm{He}_2^*(^3\mathrm{d})$−He potential, which is mainly responsible for the experimentally observed ^{3}d → ^{3}b fluorescence band shift (see Figure 5), appears similar to the atomic He*(3s)−He potential.[18] The latter interaction was shown to be responsible for the pronounced blue shift of the atomic 3s → 2p fluorescence line in liquid helium. Both potentials exhibit similar long-range maxima: 123 cm^{-1} at 5.3 Å for He* and 85 cm^{-1} at 5.8 Å for He_2^* (spherically averaged). However, the $\mathrm{He}_2^*(^3\mathrm{d})$−He interaction exhibits a farther reaching repulsive tail (*cf.* Figure 6), which is expected to produce a more pronounced pressure dependence for the ^{3}d → ^{3}b fluorescence band.

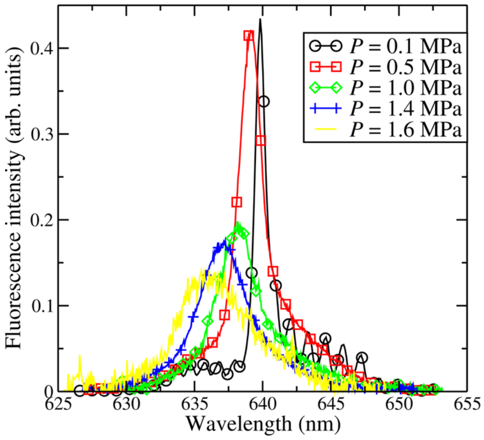

Figure 5. Experimentally observed pressure dependence of He_2^* excimer ^{3}d → ^{3}b fluorescence band in dense helium at 4.5 K. Notice the pronounced blue shift and the gradual disappearance of the rotational structure starting at 0.1 MPa. The applied current was 0.3 *μ*A and the following discharge voltages correspond to the pressures cited in the legend; *P* = 0.1 MPa, *V* = −3.5 kV; *P* = 0.5 MPa, V= −5.8 kV; *P* = 1 MPa, V = −5.7 kV; *P* = 1.4 MPa, V = −5.8 kV; *P* = 1.6 MPa, V = −6 kV.

Spectroscopy and Electron Mobility. On the basis of the previously discussed excimer−helium pair potentials, a strong blue shift of the He_2^* ^{3}d → ^{3}b fluorescence band as a function of pressure is expected, due to the increased helium density around the excimer. This is clearly confirmed by the experimental data summarized in Figure 5. The magnitude of the ^{3}d → ^{3}b blue shift is slightly larger than observed for the He* 3s (^{3}S) → 2p (^{3}P) atomic transition: 150 vs 120 cm^{-1} at 2.5 MPa, respectively.[18] The partially resolved rotational lines begin to merge into a single broad band above 0.25 MPa, which driven by the increasing interaction between the rotational and bath degrees of freedom.

To complement this spectroscopic data, electron mobility between the electrodes was also determined to assess the relative density of the system.[43−45] As the previously cited studies have shown, the mobility decreases rapidly when transitioning from the gas to the liquid phase. Figure 7 displays the observed fluorescence spectra and discharge currents of both He_2^* and He* obtained at two relatively similar pressures: 5.1 and 5.5 bar, which are both located in the supercritical fluid region of the phase diagram. Note that the current is directly proportional to the electron mobility between the two electrodes.

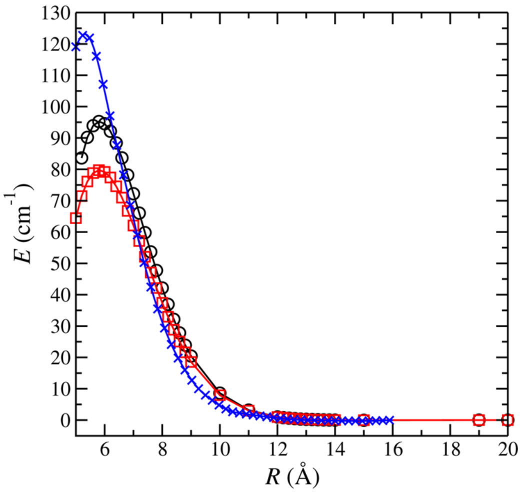

Figure 6. Magnified view of $\mathrm{He}_2^*(^3\mathrm{d})$−He potentials from CC3-EOM/basis ** calculations. Both linear (°) and T-shape (□) approaches are plotted. For comparison, the He*(3s)−He potential (×) from ref 18 is also shown.

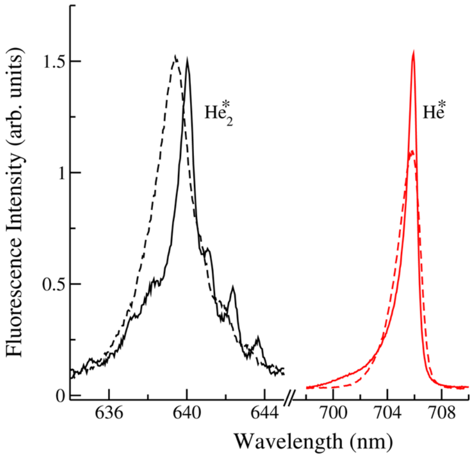

Figure 7. Fluorescence band shift for He_2^* (^{3}d → ^{3}b) at *ca.* 640 nm (left) and He* 3s (^{3}S) → 2p (^{3}P) at 706 nm (right) at 14 K. The solid lines correspond to a pressure of 5.1 bar, 30 *μ*A current, and a discharge voltage of −2.635 kV. The dotted lines correspond to a pressure of 5.5 bar, 2 *μ*A current and a discharge voltage of −3.445 kV.

The observed spectral blue shift of the He_2^* ^{3}d → ^{3}b fluorescence band at 14 K appears abruptly at the same pressure as the electron mobility decreases rapidly. However, as shown in the right panel of Figure 7, the atomic He* 3s (^{3}S) → 2p (^{3}P) line does not shift at this point yet, but only broadens slightly, and the blue tail characteristic to the gas phase disappears. On the atomic scale, both the spectral band shifts and electron mobility are expected to be strongly affected by helium density, which in turn is regulated by the pressure and temperature through the thermodynamic equation of state.

However, the existing reference data shows a rather weak dependence of density on pressure near this (P, T) point, which cannot alone account for the observed rapid changes. By solely considering the He_2^* fluorescence spectrum, one could suggest that the local surrounding of the excimer is not in complete thermodynamic equilibrium, which could cause more pronounced variations in the local density as a function of pressure and the experimentally observed abrupt change in the blue shift of the fluorescence band. However, the electron mobility is determined by helium present throughout in the region between the two electrodes, and hence it is not sensitive to such local density variations. Therefore, a more plausible explanation for this behavior is the formation of a localized state ("pre-bubble state"),[46] which takes place at the same (P, T) for both He_2^* and the electron.[24,31] In this case, He* is either not yet localized or the fluorescence shift cannot be observed, as the He*(3s)−He potential has more abrupt long-range behavior than the corresponding He_2^* potential (see Figure 6). Note that the volume occupied by He*(3s) (R = 12.6 Å at 4.5 K) in liquid helium is smaller than both $He_2^*(^3d)$ (R = 13.2 Å at 4.5 K) and the electron ($R \approx$ 15.2 Å at 0 K) at 0.5 MPa pressure.[24,31] Provided that the order of this size estimate is also valid in less dense helium, He* should not localize as easily as the other two species.

OT-DFT Lineshape Calculations. To model the pressure induced broadening of He_2^* $^3d \rightarrow {}^3b$ fluorescence band, the corresponding pair potentials between the excimer and ground state helium atom are required. A summary of the previously discussed *ab initio* potentials in the region relevant for the fluorescence line broadening are shown in Figures 6 and 8. The static liquid density profiles around freely rotating ^3d state He_2^* excimer, i.e., the spherically averaged potential, from the OT-DFT calculations at 3.0 K are shown in Figure 9 at the specified pressures. To mimic the conditions of the experiment at 4.5 K, bulk liquid densities corresponding to this temperature were employed in the calculations.[47]

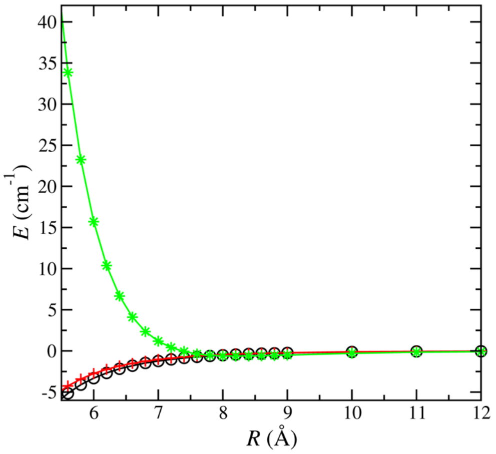

Figure 8. $He_2^*(^3b)$−He state potentials from CC3-EOM/basis ** calculations. Potentials indicated as linear (°) and T-orientation of the excimer with the π_u HOMO directed perpendicular (+), and aligned (*) to the third, impinging, helium atom.

The bubble radii, as defined by the half-bulk-density position, vary between 12.7 Å (0.1 MPa) and 10.8 Å (2.4 MPa) at 4.5 K, depending on the pressure. This implies that the ^3d state excimer bubble is much less compressible than the electron bubble.[31] The oscillatory liquid density structure appearing at the gas−liquid interface is related to the He − He correlations present in the OT functional. Note that the inclusion of the OT kinetic energy correlation functional would slightly increase these interfacial oscillations. While such oscillations do not influence the spectroscopic observables, they can, for example, increase the apparent hydrodynamic size of the excimer when it collides with the thermal excitations of the liquid. Furthermore, in the superfluid phase, the period of these oscillations correlates with the roton minimum of the dispersion relation, which suggests that they could be interpreted as localized rotons at the solvation bubble interface. At higher pressures, these oscillations become more pronounced due to the increasingly repulsive potential pressing against the liquid. Note that a presence of a bound external potential would also result in similar oscillatory liquid structure.

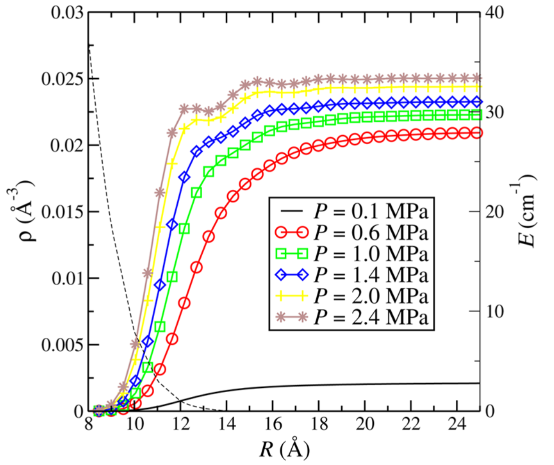

Figure 9. OT-DFT liquid helium density profiles around He_2^* excimer in the ^3d-state at 4.5 K calculated with the CC3-EOM/basis ** potentials. Note that the OT-DFT functional is evaluated at 3.0 K but the liquid density corresponding to 4.5 K is employed in the calculations. An orientationally averaged $He_2(^3d)$−He potential, *cf.* Figure 6, is shown for reference: dotted line and right ordinate.

The solvation energy of the ^3d-state excimer depends on the external pressure through the variation of the liquid density around it. To first approximation, the fluorescence band shift is dictated by the difference between the solvation energies of the initial (^3d) and final (^3b) states evaluated with the initial state liquid density around the excimer. According to eq 2, the rapid resolvation dynamics toward the final state equilibrium configuration may also contribute to the dynamic lineshift as well as the overall line shape. However, based on the initial liquid density around the ^3d state, the interaction with the ^3b state is negligible as evidenced by the calculated *ab initio* potentials (compare potentials in Figures 6 and 8). Thus, the fluorescence band shift should track the solvation energy of the initial state as a function of pressure. Since the initial ^3d state is purely repulsive, a monotonic blue shift of the fluorescence band position is expected with increasing pressure. This general trend is reflected by the experimental data shown in Figure 10.

Propagation of the ^3d state equilibrium liquid order parameter on the ^3b state potential energy surface produces the time dependent energy gap between the initial and final states (see eq 2), which can be transformed into the corresponding fluorescence spectrum representing one line within the excimer rotational band. Since the rotational lines merge into a single band even at low pressures, it is not possible to compare the line widths from the present OT-DFT

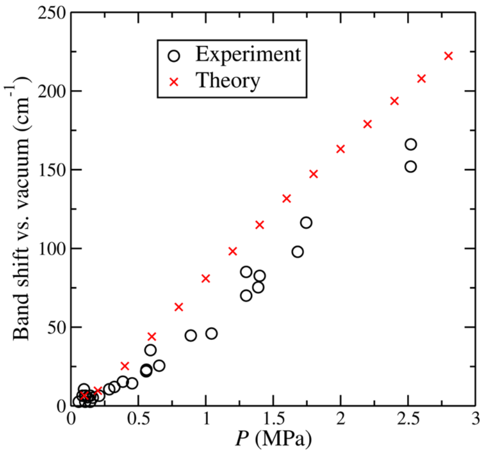

Figure 10. Comparison between experimental (○) and calculated (×) line shifts (OT-DFT with eq 1 using CC3-EOM/basis ** potentials) for He_2^* excimer $^3d \rightarrow {}^3b$ fluorescence as a function of pressure at 4.5 K.

calculations with experiments. Within the typically applicable range, $\tau = 100-300$ fs,[41] the calculated $^3d \rightarrow {}^3b$ band blue shift appeared independent of the dephasing time (see eq 3). Furthermore, the full width at half-maximum of the excimer zero-point density distribution was approximately 1 Å, which had no impact on the calculated fluorescence line shift. The results from the calculated rotational band shifts are shown in Figure 10, along with the experimental data obtained at 4.5 K. The calculations reproduce the general blue shift trend but shows some deviation that increases toward the higher pressures. This deviation appears similar to that observed previously for the pressure dependence of the atomic He*(3s) → He*(2p) transition.[18] Since this pronounced blue shift is a direct consequence of the shallow long-range repulsion in the $He_2^*(^3d)$−He pair potential (*cf.* Figure 6), the observed difference may be ascribed to a limitation in the accuracy of the calculated repulsive interaction. Other possible sources include many body effects contributing to the overall excimer−liquid interaction and the difference in the temperatures used in OT-DFT functional (3.0 K) vs experiment (4.5 K). Note that the thermal OT-DFT model has not yet been extended beyond the applied temperature in this work. To summarize, the present spectroscopic data can be used to directly interrogate the ^3d state excimer solvation energy as a function of pressure and temperature. Within the applied pressure range at 4.5 K, both He_2^* and He*[18] emit from bubble states, which require sufficiently high helium density to form. The good agreement observed between the OT-DFT simulations and the experimental fluorescence data suggests that both He_2^* and He* emit from a liquid environment at 4.5 K ($P > 0.15$ MPa) rather than directly from the hot gaseous discharge zone.

Finally, we note the possibility of filling the bound short-range pocket of the ^3d state potential with helium (see Figures 1 and 2). If the applied pressure or temperature would be sufficiently high, the surrounding ground state helium atoms could reach over the long-range barrier (see Figure 6) to fill the pocket. Since this part of the $He_2^*(^3d)$−He potential is strongly bound and the lower ^3b state is no longer flat in that region, the fluorescence band corresponding to this transition would experience very strong red shift and broadening. From the experimental point of view, this would effectively lead to quenching of the fluorescence signal. By including the high-density cutoff functional in OT-DFT,[30,34] the maximum number of helium atoms that can localize in the well around a freely rotating ^3d state excimer is approximately 17. On the basis of the discussion above, the present experiments carried out at 4.5 K observe the He_2^* $^3d \rightarrow {}^3b$ fluorescence band that originates exclusively from excimers that are solvated in the bulk portion of the liquid. This is a consequence of the fluorescence quenching that takes place in the high temperature discharge zone where high kinetic energy helium atoms are able to cross over the ^3d state barrier. For this reason, the current experiments observe *only* the minority of excimers that are formed outside the discharge zone in the bulk liquid. Note that a similar situation appears for the fluorescence that originates from the atomic He*(3s) state (*cf.* Figure 6)).[18] To conclude, due to the high temperature and pressure in the discharge zone, fluorescence originating from both He_2^* (^3d) and He* (3s) states become effectively quenched. This implies that spectroscopic experiments involving these initial electronic states can only be used to probe the state of the surrounding dense helium rather than the discharge zone itself. The electron impact process responsible for the formation of He* and He_2^* species outside the discharge zone is discussed in detail in ref 18.

■ CONCLUSIONS

We have computed the interaction of molecular excimers, He_2^*, in its various triplet electronic states with a ground state helium atom. The symmetry of these pair potentials is dictated by the Rydberg electron density due to the Pauli repulsion with the closed shell He atom. When nodal planes are present in the Rydberg orbital, the charge−induced dipole interaction with the exposed He_2^+ core produces deeply bound minima at short distances, which may result, for example, in fluorescence quenching when populated. Because of the long-range repulsive ^3d state potential, the experimentally observed $He_2^*(^3d) \rightarrow He_2^*(^3b)$ fluorescence band at 4.5 K exhibits a similar spectral blue shift with increasing pressure as the previously studied atomic He*(3s) → He*(2p) line.[18] The accuracy of the presented *ab initio* potentials was assessed by performing OT-DFT calculations to model the $^3d \rightarrow {}^3b$ fluorescence line shift. The theory slightly overestimated the blue shift but, in general, produced satisfactory agreement with the experiments. The small difference may originate either from the application of a simplified theory to model the surrounding helium bath or the presence of reduced helium density around the excimers created by corona discharge. By combining both spectroscopic and mobility data, a transition from gas phase to localized bubble state was observed to take place at a temperature of 14 K and pressure of 0.5 MPa for both He_2^* and the electron. The magnitude of the spectral shifts at 4.5 K indicate that observed He_2^* molecules emit from dense helium (i.e., bulk liquid when $P > 0.15$ MPa) rather than the gaseous high temperature discharge zone. This rather surprising observation can be explained by fluorescence quenching in this zone where high kinetic energy helium atoms are able to penetrate the short-range bound pocket around the ^3d state. In general, this implies that spectroscopy involving the previously discussed electronic transitions can only be used to probe the state of the surrounding medium rather than the discharge zone itself.

DOI: 10.1021/acs.jpca.6b08412
J. Phys. Chem. A 2016, 120, 9019−9027

■ ASSOCIATED CONTENT

Ⓢ Supporting Information

The Supporting Information is available free of charge on the ACS Publications website at DOI: 10.1021/acs.jpca.6b08412.

Tables 1−4, containing calculated triplet interaction potentials (PDF)

■ AUTHOR INFORMATION

Corresponding Author

*(S.L.F.) E-mail: steven.fiedler@fitchburgstate.edu. Telephone: 978-665-3391.

Notes

The authors declare no competing financial interest.

■ ACKNOWLEDGMENTS

Financial support from the National Science Foundation for Grants CHE-1262306 and DMR-1205734 to J.E. is gratefully acknowledged.

■ REFERENCES

(1) Gallagher, T. *Simple Dielectric Liquids: Mobility Conduction, And Breakdown*; Oxford science research papers; Oxford University Press: 1975.

(2) Allen, A. O. *Drift Mobilities and Conduction Band Energies of Excess Electrons in Dielectric Liquids*; Nat. Std. Ref. Data Series NSRDS-NBS 58; National Bureau of Standards: Washington DC, 1976.

(3) Lewis, T. J. Basic electrical processes in dielectric liquids. *IEEE Trans. Dielectr. Electr. Insul.* **1994**, *1*, 630−643.

(4) Zahn, M. *Wiley Encyclopedia of Electrical and Electronics Engineering*;. John Wiley & Sons, Inc.: 2001.

(5) André, D. Conduction and breakdown initiation in dielectric liquids. *2011 IEEE International Conference on Dielectric Liquids*; 2011; pp 1−11.

(6) Schmidt, W. F., Illenberger, E., Eds. *Electronic Excitations in Liquefied Rare Gases*; American Scientific Publishers: 2005.

(7) Lesaint, O.; Gournay, P. On the Gaseous Nature of Positive Filamentary Streamers in Hydrocarbon Liquids. I: Influence of the Hydrostatic Pressure on the Propagation. *J. Phys. D: Appl. Phys.* **1994**, *27*, 2111−2116.

(8) Kolb, J. F.; Joshi, R. P.; Xiao, S.; Schoenbach, K. H. Streamers in Water and Other Dielectric Liquids. *J. Phys. D: Appl. Phys.* **2008**, *41*, 234007.

(9) Bruggeman, P.; Leys, C. Non-thermal Plasmas in and in Contact with Liquids. *J. Phys. D: Appl. Phys.* **2009**, *42*, 053001.

(10) Sima, W.; Jiang, C.; Lewin, P.; Yang, Q.; Yuan, T. Modeling of the Partial Discharge Process in a Liquid Dielectric: Effect of Applied Voltage, Gap Distance, and Electrode Type. *Energies* **2013**, *6*, 934−952.

(11) Kattan, R.; Denat, A.; Bonifaci, N. Formation of Vapor Bubbles in Nonpolar Liquids Initiated by Current Pulses. *IEEE Trans. Electr. Insul.* **1991**, *26*, 656−662.

(12) Gallimberti, I.; Hepworth, J. K.; Klewe, R. C. Spectroscopic Investigation of Impulse Corona Discharges. *J. Phys. D: Appl. Phys.* **1974**, *7*, 880−898.

(13) Simek, M.; Babicky, V.; Clupek, M.; DeBenedictis, S.; Dilecce, G.; Sunka, P. Excitation of $N_2(C^3\Pi_u)$ and NO(A $^2\Sigma^+$) States in a Pulsed Positive Corona Discharge in N_2, N_2-O_2 and N_2-NO Mixtures. *J. Phys. D: Appl. Phys.* **1998**, *31*, 2591−2602.

(14) Simek, M. The Modelling of Streamer-induced Emission in Atmospheric Pressure, Pulsed Positive Corona Discharge: N_2 Second Positive and NO-γ Systems. *J. Phys. D: Appl. Phys.* **2002**, *35*, 1967−1980.

(15) Bonifaci, N.; Denat, A. Spectral Analysis of Light Emitted by Prebreakdown Phenomena in Nonpolar Liquids and Gases. *IEEE Trans. Electr. Insul.* **1991**, *26*, 610−614.

(16) Bonifaci, N.; Denat, A. Electron and Light Emissions in Liquid Argon and Liquid Methane in a Divergent Electric Field. *Nucl. Instrum. Methods Phys. Res., Sect. A* **1993**, *327*, 78−80.

(17) Denat, A.; Bonifaci, N.; Nur, M. Spectral Analysis of the Light Emitted by Streamers in Hydrocarbon Liquids. *IEEE Trans. Dielectr. Electr. Insul.* **1998**, *5*, 382−387.

(18) Bonifaci, N.; Aitken, F.; Atrazhev, V. M.; Fiedler, S. L.; Eloranta, J. Experimental and Theoretical Characterization of the Long-range Interaction Between He*(3s) and He(1s). *Phys. Rev. A: At., Mol., Opt. Phys.* **2012**, *85*, 042706.

(19) Koch, H.; Christiansen, O.; Jørgensen, P.; Olsen, J. Excitation Energies of BH, CH_2 and Ne in Full Configuration Interaction and the Hierarchy CCS, CC2, CCSD and CC3 of Coupled Cluster Models. *Chem. Phys. Lett.* **1995**, *244*, 75−82.

(20) Christiansen, O.; Koch, H.; Jørgensen, P. Response Functions in the CC3 Iterative Triple Excitation Model. *J. Chem. Phys.* **1995**, *103*, 7429−7441.

(21) Boys, S. F.; Bernardi, F. The Calculation of Small Molecular Interactions by the Differences of Separate Total Energies. Some Procedures with Reduced Errors. *Mol. Phys.* **1970**, *19*, 553−566.

(22) Turney, J. M.; Simmonett, A. C.; Parrish, R. M.; Hohenstein, E. G.; Evangelista, F. A.; Fermann, J. T.; Mintz, B. J.; Burns, L. A.; Wilke, J. J.; Abrams, M. L.; et al. Psi4: An Open-source Ab Initio Electronic Structure Program. *Wiley Interdiscip. Rev. Comput. Mol. Sci.* **2012**, *2*, 556−565.

(23) Fiedler, S. L.; Eloranta, J. Interaction of Helium Rydberg State Atoms with Superfluid Helium. *J. Low Temp. Phys.* **2014**, *174*, 269−283.

(24) Eloranta, J.; Schwentner, N.; Apkarian, V. A. Structure and Energetics of He_2^* Bubble-states in Superfluid ^{4}He. *J. Chem. Phys.* **2002**, *116*, 4039−4053.

(25) Sunil, K. K.; Lin, J.; Siddiqui, H.; Siska, P. E.; Jordan, K. D.; Shepard, R. Theoretical Investigation of the $a^3\Sigma_u{}^+$, $A^1\Sigma_u{}^+$, $c^3\Sigma_g{}^+$, and $C^1\Sigma_g{}^+$ Potential Energy Curves of He_2 and of He*(2^1S, 2^3S)+He Scattering. *J. Chem. Phys.* **1983**, *78*, 6190−6202.

(26) Deguilhem, B. Calcul Ab Initio D’observables Pour les Condensats D’hélium Métastable. Ph.D. Thesis, Université de Toulouse: 2009.

(27) Ancilotto, F.; Faccin, F.; Toigo, F. Wetting Transitions of ^{4}He on Alkali-metal Surfaces from Density-functional Calculations. *Phys. Rev. B: Condens. Matter Mater. Phys.* **2000**, *62*, 17035−17042.

(28) Dalfovo, F.; Lastri, A.; Pricaupenko, L.; Stringari, S.; Treiner, J. Structural and Dynamical Properties of Superfluid Helium: A Density-functional Approach. *Phys. Rev. B: Condens. Matter Mater. Phys.* **1995**, *52*, 1193−1209.

(29) Grau, V.; Barranco, M.; Mayol, R.; Pi, M. Electron Bubbles in Liquid Helium: Density Functional Calculations of Infrared Absorption Spectra. *Phys. Rev. B: Condens. Matter Mater. Phys.* **2006**, *73*, 064502.

(30) Ancilotto, F.; Barranco, M.; Pi, M. Motion of Electrons in Liquid ^{4}He. *Phys. Rev. B: Condens. Matter Mater. Phys.* **2010**, *82*, 014517.

(31) Eloranta, J.; Apkarian, V. A. A Time Dependent Density Functional Treatment of Superfluid Dynamics: Equilibration of the Electron Bubble in Superfluid ^{4}He. *J. Chem. Phys.* **2002**, *117*, 10139−10150.

(32) Aitken, F.; Bonifaci, N.; von Haeften, K.; Eloranta, J. Theoretical Modeling of Electron Mobility in Superfluid ^{4}He. *J. Chem. Phys.* **2016**, *145*, 044105.

(33) Fiedler, S. L.; Mateo, D.; Aleksanyan, T.; Eloranta, J. Theoretical Modeling of Ion Mobility in Superfluid ^{4}He. *Phys. Rev. B: Condens. Matter Mater. Phys.* **2012**, *86*, 144522.

(34) Leal, A.; Zhang, X.; Barranco, M.; Cargnoni, F.; Hernando, A.; Mateo, D.; Mella, M.; Drabbels, M.; Pi, M. Dynamics of Photoexcited Ba^+ Cations in ^{4}He Nanodroplets. *J. Chem. Phys.* **2016**, *144*, 094302.

(35) Lehtovaara, L.; Kiljunen, T.; Eloranta, J. Efficient Numerical Method for Simulating Static and Dynamic Properties of Superfluid Helium. *J. Comput. Phys.* **2004**, *194*, 78−91.

(36) Lehtovaara, L.; Toivanen, J.; Eloranta, J. Solution of Time-independent Schrödinger Equation by the Imaginary Time Propagation Method. *J. Comput. Phys.* **2007**, *221*, 148−157.

(37) Lehtovaara, L.; Mateo, D.; Eloranta, J. High-level Library for Managing 1-D, 2-D and 3-D Regular Grids. Available on: http://sourceforge.net/projects/libgrid/, 2016.

(38) Lehtovaara, L.; Mateo, D.; Eloranta, J. Implementation of the Orsay-Trento Density Functional for Describing Superfluid Helium. Available on: http://sourceforge.net/projects/libdft/, 2016.

(39) Mukamel, S. *Priciples of Nonlinear Optics and Spectroscopy*, 3rd ed.; Oxford Series in Optical and Imaging Sciences (Book 6); Oxford University Press: New York, 1995.

(40) Eloranta, J.; Seferyan, H. Y.; Apkarian, V. A. Time-domain Analysis of Electronic Spectra in Superfluid ^{4}He. *Chem. Phys. Lett.* **2004**, *396*, 155−160.

(41) Popov, E. A.; Eloranta, J. Copper Dimer Interactions on a Thermomechanical Superfluid ^{4}He Fountain. *J. Chem. Phys.* **2015**, *142*, 204704.

(42) Eloranta, J.; Apkarian, V. A. The Triplet He_2^* Rydberg States and Their Interaction Potentials with Ground State He Atoms. *J. Chem. Phys.* **2001**, *115*, 752−760.

(43) Harrison, H. R.; Sander, L. M.; Springett, B. E. Electron Mobility and Localization in Dense He^4 gas. *J. Phys. B: At. Mol. Phys.* **1973**, *6*, 908−917.

(44) Schwarz, K. W. Electron Localization in Dense Helium Gas: New Experimental Results. *Phys. Rev. B: Condens. Matter Mater. Phys.* **1980**, *21*, 5125−5136.

(45) Bartholomew, J.; Hall, R.; Berne, B. J. Behavior of an Electron in Helium Gas. *Phys. Rev. B: Condens. Matter Mater. Phys.* **1985**, *32*, 548−551.

(46) Hernandez, J. P. Electron Self-trapping in Liquids and Dense Gases. *Rev. Mod. Phys.* **1991**, *63*, 675−697.

(47) Arp, V. D.; McCarty, R. D.; Friend, D. G. *Thermophysical Properties of Helium-4 from 0.8 to 1500 K with Pressures to 2000 MPa*; NIST Technical Note 1334 (revised) NIST: Boulder, CO, 1998.

DOI: 10.1021/acs.jpca.6b08412
J. Phys. Chem. A 2016, 120, 9019−9027